

Impact of Oxygen Vacancies in Josephson Junction on Decoherence of Superconducting Qubits

Hanqin Bai,¹ Shi-Yao Hou,^{1,*} and Mu Lan²

¹College of Physics and Electronic Engineering, Center for Computational Sciences, Sichuan Normal University, Chengdu 610068, China

²Sichuan Province Key Laboratory of Optoelectronic Sensor Devices and Systems, College of Optoelectronic Engineering, Chengdu University of Information Technology, Chengdu 610225, China, Sichuan Meteorological Optoelectronic Sensor Technology and Application Engineering Research Center, Chengdu University of Information Technology, Chengdu 610225, China

(Dated: March 13, 2026)

Superconducting quantum circuits are promising platforms for scalable quantum computing, where qubit coherence is critically determined by microscopic defects in the oxide tunneling barrier of Josephson junctions. Amorphous Al_2O_3 is widely used as a barrier material, but under irradiation, oxygen vacancy (V_O) defects are readily generated, introducing noise sources that accelerate qubit decoherence. We systematically investigate the structural characteristics and electronic impact of V_O defects in amorphous Al_2O_3 using first-principles calculations and *ab initio* molecular dynamics. Our results show that both the coordination environment and concentration of V_O s strongly influence electrical conductivity. In particular, two- and three-coordinated V_O s, unique to the amorphous structure, enhance conductivity more than conventional four-coordinated vacancies. Increasing V_O concentration amplifies conductivity fluctuations, which we link to critical current noise in Josephson junctions. Using a noise model, we estimate that higher V_O densities lead to shorter qubit coherence times. These findings provide insights for radiation-hard design of superconducting quantum devices.

I. INTRODUCTION

High-performance superconducting qubits are essential for realizing large-scale practical quantum computing [1]. In recent years, continuous improvements in gate fidelity and coherence times have enabled superconducting quantum processors to integrate hundreds of qubits, laying the foundation for scalable universal quantum computation [2]. Nevertheless, decoherence remains a key factor limiting long-term scalability. Extensive studies show that decoherence predominantly originates from defect-related states in materials, such as two-level systems (TLSs), charge noise, flux noise, radio-frequency energy leakage, and parasitic couplings [3–9]. In particular, microscopic defects in device materials—especially in the Al_2O_3 insulating layer—introduce low-frequency noise that degrades qubit energy-level stability and gate fidelity. Impurity states associated with hydrogen-related defects [10, 11] and oxygen vacancies (V_O) [12–14] have been identified as major contributors to such noise sources.

To mitigate decoherence, various strategies have been proposed, including suppressing the coupling between defects and the environment [15], as well as optimizing fabrication processes—for example, employing thermal annealing to reduce V_O formation [16, 17] and thereby suppress noise. Previous studies demonstrate that hydrogen impurities can form $\text{O}-\text{H}\cdots\text{O}$ tunneling configurations, giving rise to noise in dielectric materials [11]. In addition, hydrogen binds with aluminum vacancies

to form $V_{\text{Al}}-\text{H}$ complexes, which constitute dominant defects in oxide layers and significantly deteriorate material performance [10]. These findings highlight the importance of understanding microscopic noise origins and defect structures for controlling decoherence in superconducting qubits.

Oxygen vacancies, in particular, play a crucial role in determining the electrical properties of oxide materials. Previous work shows that the microscopic structure of V_O s strongly influences charge transport behavior [14, 18]. Due to its excellent insulating properties, amorphous Al_2O_3 is commonly used as the oxide barrier in Josephson junctions. However, under high-energy irradiation, Al–O bonds in Al_2O_3 can break, leading to Al dangling bonds at metal-oxide interfaces and V_O s within the oxide bulk [19–21]. X-ray photoelectron spectroscopy measurements indicate that V_O concentration increases with irradiation dose. In addition, oxides may trap excess charges, altering local charge density and consequently modifying material properties. It has also been reported that variations in the position, distribution, and concentration of V_O s within the tunnel barrier significantly affect the local density of states (LDOS), while Coulomb repulsion between Al ions near vacancies promotes electron delocalization and modifies electrical conductivity. These studies reveal that V_O s can alter electron tunneling pathways and conductive channels in Josephson junctions, thereby influencing transport behavior.

Despite these advances, direct investigations of the electronic structure of irradiation-induced V_O s in amorphous oxides, as well as their impact on transport properties and qubit decoherence mechanisms, remain limited. A systematic understanding of how

* hshiyao@sicnu.edu.cn

irradiation-induced V_{OS} in amorphous Al_2O_3 affect charge transport and coherence is therefore highly desirable for improving coherence and radiation tolerance of Al/ AlO_x /Al Josephson junctions.

In this work, we employ density functional theory (DFT) to investigate the electronic structure of irradiation-induced V_{OS} in amorphous Al_2O_3 and explain how the coordination environment and concentration of vacancies influence charge transport properties. We first construct realistic amorphous models via *ab initio* molecular dynamics and validate their structural properties. We then systematically analyze the effect of V_O coordination (2-, 3-, and 4-fold) and concentration on electronic structure and conductivity. Finally, we link the conductivity fluctuations to critical current noise in Josephson junctions and provide quantitative estimates of qubit decoherence times. Our results demonstrate that both coordination environment and concentration of V_{OS} are critical factors determining qubit coherence, offering guidance for material design and defect engineering in superconducting quantum devices.

II. THEORETICAL DETAILS

To construct an amorphous Al_2O_3 structure, we employed a melt-quench procedure via *ab initio* molecular dynamics (AIMD) simulations using the Vienna *ab initio* simulation package (VASP). This approach effectively reproduces, at the atomic scale, the experimental process of obtaining amorphous materials through high-temperature melting followed by rapid quenching, thereby providing a reliable model for investigating their local structural and electronic properties. Using a supercell containing 64 Al atoms and 96 O atoms, all simulations were performed in the NVT ensemble with the Nose-Hoover thermostat, using an integration time step of 0.5 fs. First, the system temperature was rapidly increased from 300 K to 4000 K in 100 K increments at a heating rate of 100 K/ps to melt the crystalline structure. Subsequently, the temperature was maintained at 4000 K for 0.5 ps. Finally, the system was cooled from 4000 K to 300 K at a cooling rate of 100 K/ps to obtain the amorphous Al_2O_3 structure.

Spin-polarized first-principles calculations were performed within the density functional theory (DFT) framework using VASP [22, 23] and projector augmented wave (PAW) [24, 25] pseudopotentials. The exchange-correlation interactions were treated with the strongly constrained and appropriately normed semilocal density functional (SCAN) [26] meta-generalized gradient approximation (metaGGA) for geometry optimization, as it provides an accurate description of bond lengths and coordination in amorphous oxides. To address the underestimation of bandgaps, electronic band structures and densities of states were calculated using the HSE06 [27, 28] hybrid functional, which incorporates 45% nonlocal Hartree-Fock exchange. The

electronic configurations were set as $3s^23p^1$ for Al and $2s^22p^4$ for O. A kinetic energy cutoff of 520 eV was employed. Electronic energy minimization was achieved with a tolerance of 10^{-6} eV, while ionic relaxation proceeded until the force on each atom was below 0.02 eV/Å.

III. MODEL CONSTRUCTION AND STRUCTURAL VALIDATION

The constructed amorphous Al_2O_3 supercell contains 160 atoms (64 Al and 96 O), with a total volume of 1341 Å³ and a density of 4.04 g/cm³. The calculated band gap of the amorphous Al_2O_3 model is approximately 6.84 eV, which is consistent with experimental band gaps reported for amorphous Al_2O_3 films (6–7 eV) [29, 30]. To investigate the structural characteristics and verify the reliability of the model, we analyzed the pair correlation function (PCF), bond lengths, and coordination distribution. The final ten configurations from the molecular dynamics trajectories were averaged, and the averaged atomic positions were used to compute the atomic spatial correlations.

The pair correlation functions $g_{ab}(r)$ in a binary system are defined such that, sitting on one atom of species a , the probability of finding one atom of species b in a spherical shell between r and $r + \Delta r$ is

$$\langle n_{a,b}(r, r + \Delta r) \rangle = \rho_b 4\pi r^2 g_{a,b}(r) \Delta r,$$

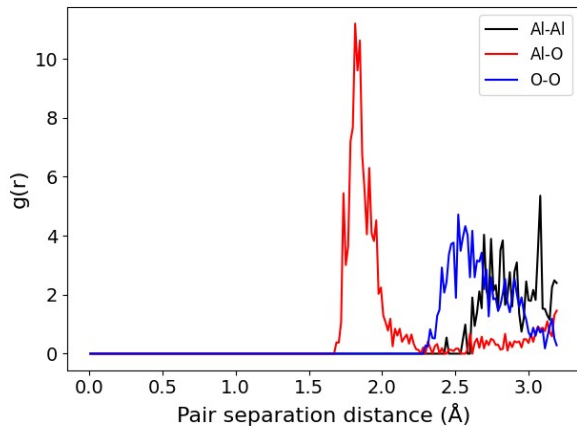
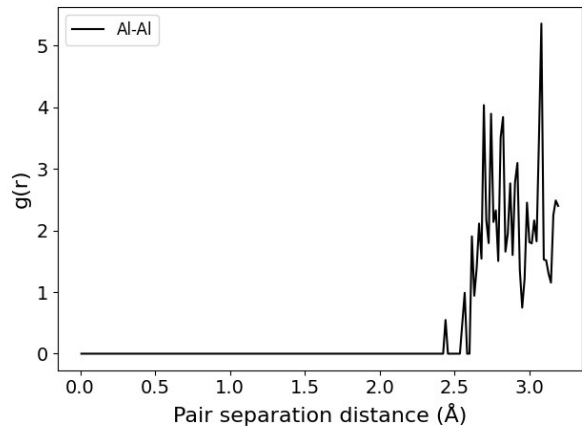
where $\rho_b = N_b/V$ is the number density of species b , and N_b is the total number of atoms of species b [31].

In Fig. 1a, the PCF of amorphous Al_2O_3 exhibits a pronounced first peak, corresponding to the nearest-neighbor atomic correlations. This indicates distinct short-range order in the system, primarily arising from the strong Al–O bonding within the network structure. Beyond the first peak, the intensity gradually decreases and becomes significantly broadened, reflecting the long-range structural disorder characteristic of the amorphous phase. Figs. 1b–1d display the Al–Al, Al–O, and O–O pair correlation functions, respectively. Based on the positions of the first peaks, the estimated nearest-neighbor distances are approximately 3.08 ± 0.05 Å for Al–Al, 1.81 ± 0.10 Å for Al–O, and 2.52 ± 0.20 Å for O–O, with uncertainties estimated from the half-width at half-maximum (HWHM).

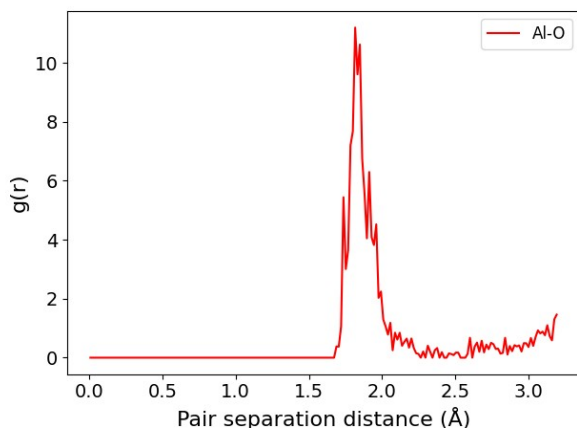
A useful supplementary information can be obtained by integrating around the first peak in the PCF, which provides the average coordination number n_{ab} [32]:

$$n_{ab}(R) = 4\pi\rho_b \int_0^R g_{ab}(r) r^2 dr,$$

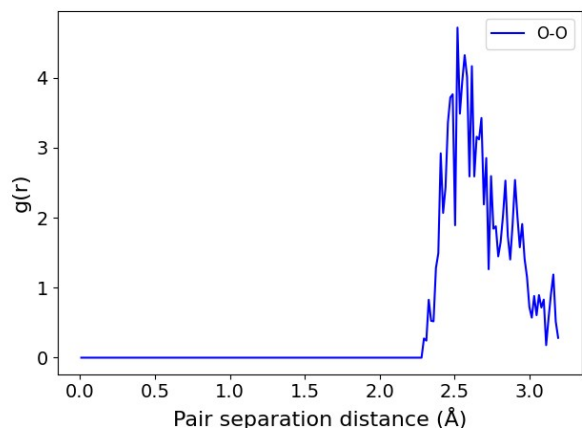
where R is a cutoff, usually chosen as the position of the minimum after the first peak of $g_{ab}(r)$. Within the

(a) Total pair correlation function for amorphous Al_2O_3 .

(b) Al-Al pair correlation function.



(c) Al-O pair correlation function.



(d) O-O pair correlation function.

FIG. 1: Partial pair correlation functions for amorphous Al_2O_3 .

cutoff distances $R_{\text{Al-Al}} = 3.3 \text{ \AA}$, $R_{\text{Al-O}} = 2.6 \text{ \AA}$, and $R_{\text{O-O}} = 3.2 \text{ \AA}$, the results show that each Al atom has, on average, 6.62 Al neighbors and 5.78 O neighbors, while each O atom has an average of 3.85 Al neighbors and 11.08 O neighbors.

We further analyzed the coordination number distributions for different atoms and plotted the corresponding histograms (Figs. 2a–2d). For Al atoms, those with coordination numbers of 4, 5, and 6 account for approximately 74% of the total, with sixfold-coordinated Al atoms being the most abundant, indicating that octahedral configurations are dominant. Al atoms with coordination numbers of 2 or 3 constitute only about 15%. For O atoms, the coordination number distribution shows that 29% are twofold-coordinated, 30% are threefold-coordinated, and 31% are fourfold-coordinated, while only about 10% of O atoms are onefold or fivefold coordinated. The coordination number distributions of Al-Al and O-O pairs are relatively broad, with coordination numbers of 5 and 7 being the most frequent for Al-Al, and 6, 7, 9, and 10 for O-O. The observed deviations

may arise from the accuracy of the cutoff distance.

Lamparter’s experimental measurements [33] of amorphous Al_2O_3 reported Al-O, Al-Al, and O-O bond lengths of 1.8, 3.2, and 2.8 \AA , respectively, with an Al coordination number of 4.1. Oka’s study [34] on anodically oxidized amorphous Al_2O_3 revealed that, in low-density porous films, the Al-O bond length is about 1.8 \AA and Al atoms are tetrahedrally coordinated, while in high-density nonporous films, the Al-O bond length increases to about 1.9 \AA and Al atoms become octahedrally coordinated.

Table I summarizes and compares our simulation results with available experimental data. Experiments generally show Al-O bond lengths ranging from 1.8 to 1.9 \AA and Al coordination numbers between 4.1 and 4.8. It is widely accepted that the amorphous Al_2O_3 network consists primarily of tetrahedral (AlO_4) and octahedral (AlO_6) polyhedral units, with their relative proportions depending on the preparation method. Experimental evidence indicates that both coordination number and polyhedral proportion are correlated with sample den-

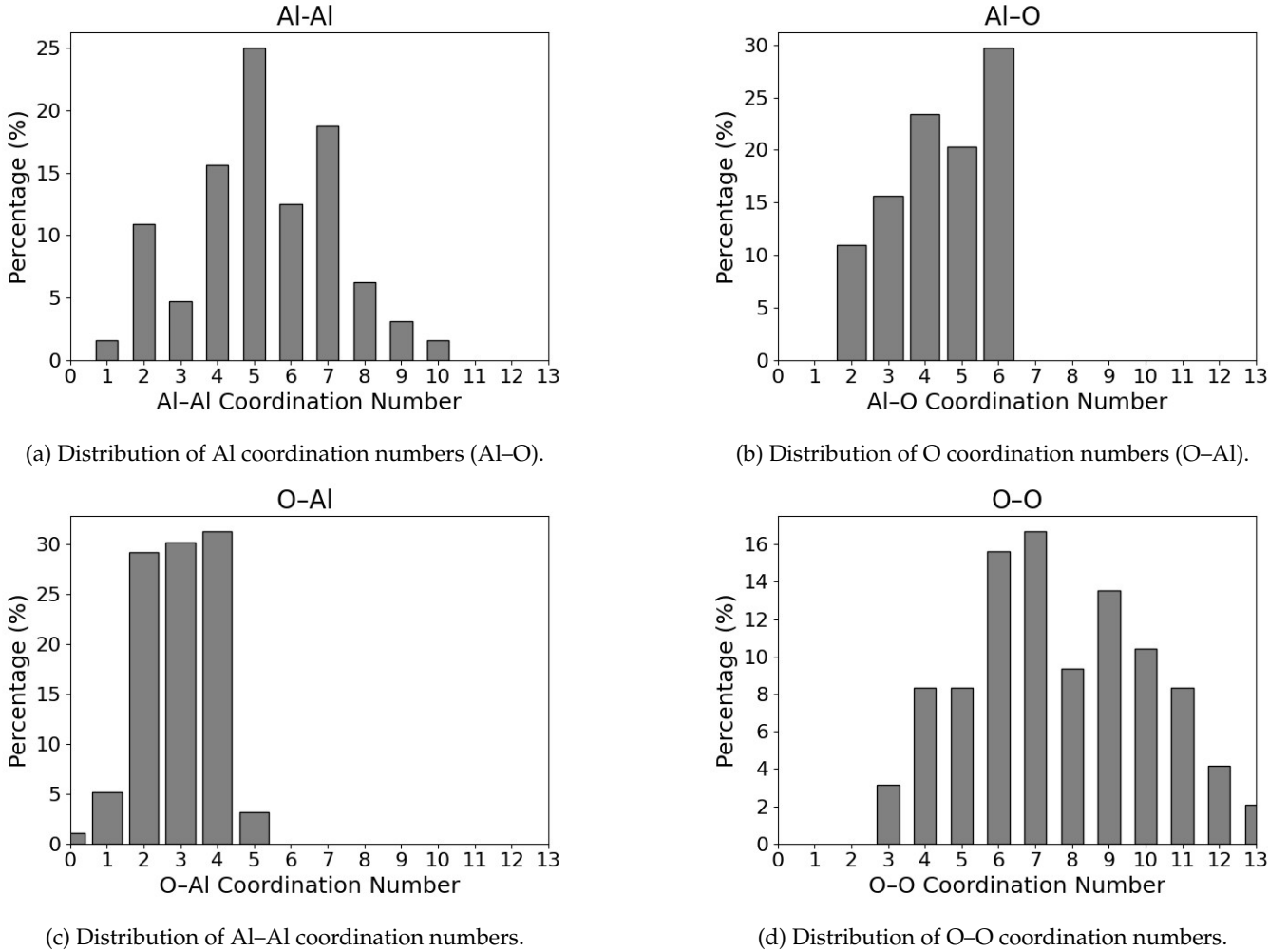


FIG. 2: Distribution of Al and O nearest-neighbor coordination in amorphous Al_2O_3 .

TABLE I: Comparison of our simulation results with available experimental data for amorphous Al_2O_3 . Bond lengths r (in \AA) and coordination pair numbers n are given for each atomic pair.

	Lamparter and Kniep		Oka		Gonzalo and Börje		This work	
	r (\AA)	n	r (\AA)	n	r (\AA)	n	r (\AA)	n
Al-O	1.8 ± 0.21	4.1	1.85	4.64/4.81	1.76 ± 0.1	4.25	1.81 ± 0.1	5.78
O-O	2.8 ± 0.58	8.5	-	-	2.75 ± 0.2	9.47	2.52 ± 0.2	11.08
Al-Al	3.2 ± 0.55	6	-	-	3.1 ± 0.21	8.26	3.08 ± 0.05	6.62

sity. Gonzalo and Börje [31] conducted simulations over a density range of $3.0\text{--}3.3 \text{ g/cm}^3$ and found that, although bond lengths and bond angle distributions show minor variations, the coordination and ring statistics change markedly with density: as density increases, the number of overcoordinated polyhedra (AlO_5 and AlO_6) rises, whereas undercoordinated polyhedra (AlO_3 and AlO_4) decrease. Therefore, our results are consistent with experimental and theoretical observations [30, 32].

IV. ELECTRONIC STRUCTURE AND TRANSPORT PROPERTIES

Based on H.P. Zhu [21] and Man Ding's [19, 20] findings, oxygen vacancies are generated in Al_2O_3 under irradiation, with vacancy concentration increasing with dose [19]. Here, vacancies are assumed to be irradiation-induced rather than intrinsic or fabrication-related.

A. Influence of V_O Coordination Number on Electrical Conductivity

Unlike crystalline Al_2O_3 , the structure of amorphous Al_2O_3 features regional disorder, and irradiation often induces V_O s with different coordination numbers. The coordination number of a V_O not only determines the depth of the associated defect levels but also affects the strength of the local electrostatic potential perturbation and its capability to modulate charge carrier transport. To systematically investigate how the coordina-

tion environment of V_{O_s} affects electrical conductivity, we constructed specific V_O defect models by removing oxygen atoms with different coordination numbers (2-fold, 3-fold, and 4-fold coordination) in amorphous Al_2O_3 . To eliminate structural bias, oxygen vacancies of each type were generated through random selection while keeping all other structural conditions identical, enabling a direct comparison of the independent effects of vacancy coordination on electrical conductivity. The electronic structure was calculated using the Tran-Blaha modified Becke-Johnson (TB-MBJ) exchange potential. Based on the obtained electronic band structure, the conductivity was evaluated using the semiclassical Boltzmann transport theory within the constant relaxation time approximation. Note that within this approximation, the calculated conductivity σ is proportional to the relaxation time τ , and we report the quantity σ/τ (with units $\Omega^{-1}m^{-1}s^{-1}$), which reflects the intrinsic electronic transport properties apart from scattering time.

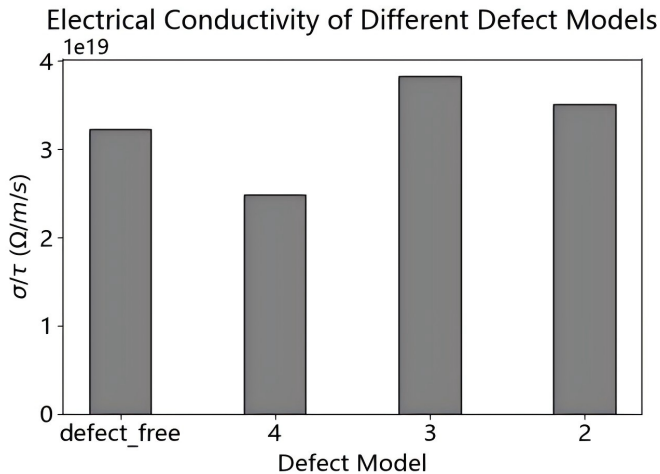


FIG. 3: Electrical conductivity (σ/τ) comparison of amorphous Al_2O_3 models with different V_O coordination environments.

In the three models, randomly selected oxygen atoms with coordination numbers of 4, 3, and 2 were removed, respectively. We then calculated the electrical conductivity of each model. As shown in Fig. 3, when the number of vacancies remains constant, the influence of different coordination numbers on conductivity is significant. The defect-free model has a conductivity of $3.23 \times 10^{19} \Omega^{-1}m^{-1}s^{-1}$. After introducing a 3-coordinated V_O , the conductivity increases significantly to $3.83 \times 10^{19} \Omega^{-1}m^{-1}s^{-1}$, a value comparable to that of the 2-coordinated vacancy model. Conversely, removing a 4-coordinated oxygen atom results in a significant reduction in conductivity to $2.48 \times 10^{19} \Omega^{-1}m^{-1}s^{-1}$. This may be attributed to the fact that, in crystalline Al_2O_3 , oxygen atoms predominantly adopt a 4-fold coordination, and most oxygen atoms in the constructed amorphous structure also maintain this coordination.

As a result, introducing a vacancy at a 4-coordinated site tends to preserve the material's insulating nature.

We further compared the conductivity spectra of the four models (Fig. 4) and observed significant differences in the low-frequency region among the V_O models with different coordination. Specifically, the conductivity spectrum of the 4-coordinated V_O model remains relatively flat at low frequencies, with only a weak peak appearing near 0 eV (Fig. 4b). This indicates that the defect states introduced by 4-coordinated V_{O_s} are relatively deep or highly localized, resulting in a negligible contribution to the overall electrical conductivity. In contrast, the 3-coordinated model exhibits a notable increase in conductivity in the low-frequency region (< 0.1 eV) (Fig. 4c). Moreover, the 2-coordinated model shows multiple peaks in the low-frequency range (Fig. 4d), indicating that the defects may introduce shallow donor states, providing multiple effective channels for the generation of free charge carriers.

To clarify the physical origin of the observed conductivity trends, we further compare the defect level distributions of the four models, as shown in Fig. 5. In the 4-coordinated oxygen vacancy model, the defect level is located closer to the valence band, corresponding to a deep donor state with strong electron localization. Such localized states contribute negligibly to electrical conduction and may even act as hole traps, resulting in a conductivity lower than that of the defect-free model. In contrast, the chemical environments of 2- and 3-coordinated oxygen atoms, which are unique to the amorphous structure, are intrinsically less stable. Upon vacancy formation, these defects introduce shallow donor levels within the band gap. In particular, the defect level associated with the 3-coordinated vacancy lies closer to the conduction band minimum, while the 2-coordinated model introduces multiple defect levels, some of which are also located near the conduction band minimum. These features indicate a greater tendency to release free electrons and provide additional carrier transport pathways, thereby enhancing electrical conductivity. Nevertheless, compared with the 3-coordinated model, the 2-coordinated model also contains relatively deeper defect levels. The electronic structure results are consistent with the observed conductivity trends.

To further investigate how oxygen vacancies regulate the local electrostatic potential distribution in amorphous Al_2O_3 , we performed planar-slice visualizations of the potential near the defects. Fig. 6a shows the local electrostatic environment of a 4-coordinated oxygen atom in the defect-free model, while Fig. 6b shows the potential slice after removing this oxygen atom, using the nearest neighbor atom to the defect site as the center, with the $x = 0$ plane as the slicing plane. A comparison of these two panels reveals that, in the absence of defects, the equipotential contours are relatively symmetric and form regular circular potential wells. After the introduction of the V_O , the potential well near

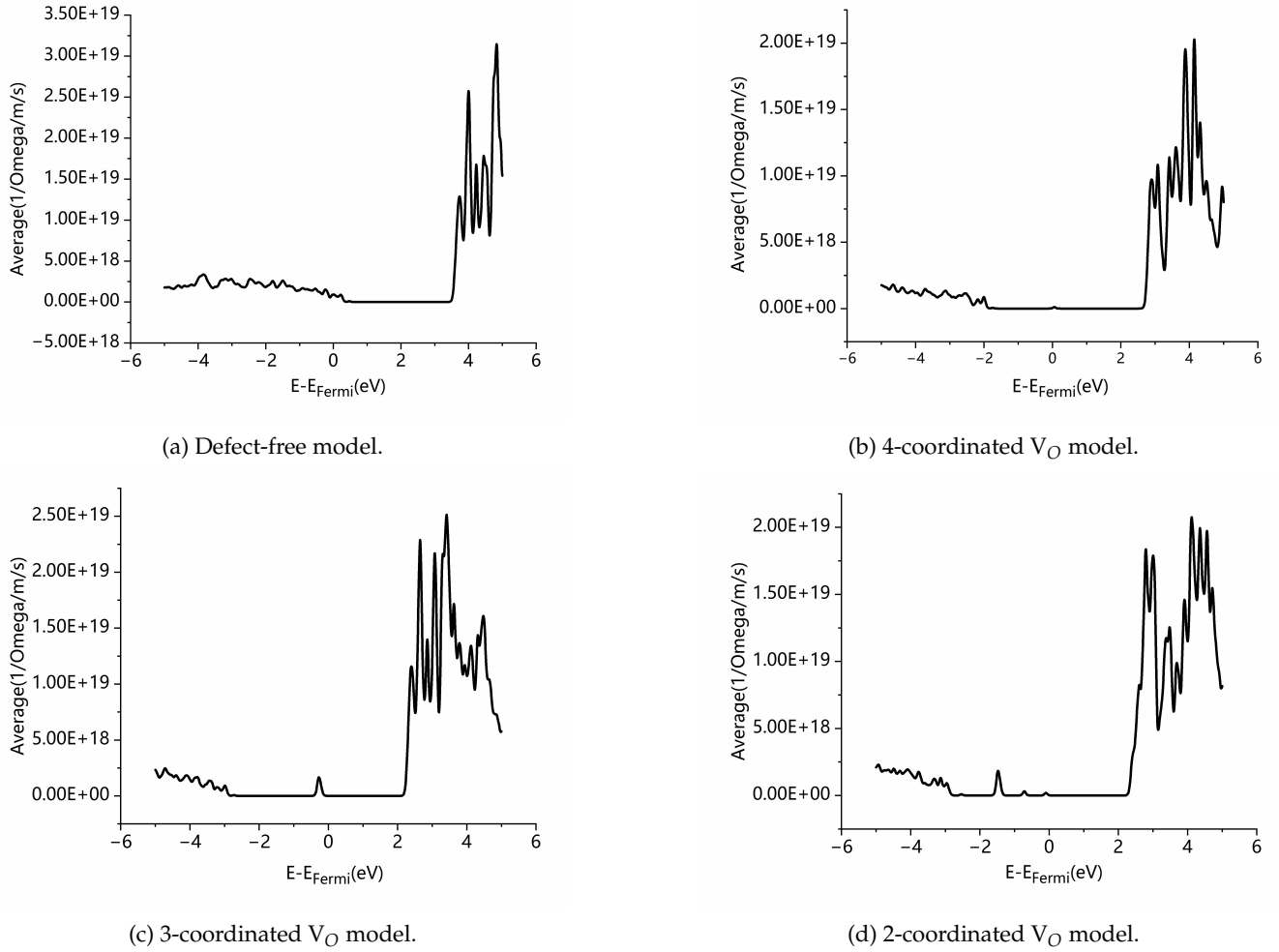


FIG. 4: Electrical conductivity spectra (σ/τ) for amorphous Al_2O_3 models with different V_O coordination environments.

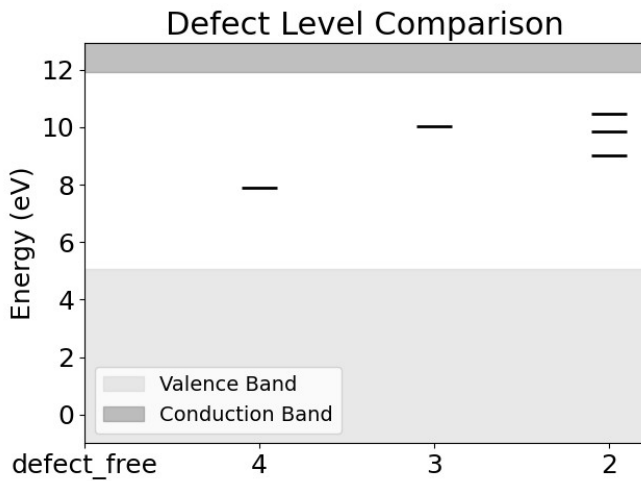


FIG. 5: Defect level distributions for amorphous Al_2O_3 models with different V_O coordination environments.

the defect remains approximately circular, while regions around Al atoms exhibit overlapping potential wells. Meanwhile, the potential depth at local Al and O sites increases, indicating a reconstruction of the local electrostatic potential induced by the defect. Figs. 6c and 6d display the electrostatic potential slices of a 3-coordinated oxygen atom in the defect-free model and after vacancy formation, respectively (with $x = 0$ as the slicing plane). In the defect-free case, the equipotential contours are symmetric and circular. Upon the introduction of a 3-coordinated V_O , the equipotential contours evolve into irregular potential-well patterns, particularly around oxygen sites, where the equipotential lines become highly distorted and the depth of the local potential wells is reduced. In contrast, overlapping potential wells and an increased potential depth are observed around local Al atoms, which may originate from enhanced Coulomb repulsion between neighboring Al ions. This behavior reflects an overall enhancement of the local Coulomb potential and an increase in

its spatial gradient. For the 2-coordinated oxygen vacancy, shown in Figs. 6e and 6f, the introduction of the defect leads to pronounced irregular distortions of the equipotential contours around oxygen atoms, accompanied by a reduction in the local potential well depth and an increased potential difference relative to surrounding regions. Such modifications of the electrostatic potential landscape can increase the probability of electron transitions when carriers traverse the defective barrier, thereby altering the transport properties of the system.

The introduction of V_O s leads to increased electron tunneling probability in the oxide barrier layer and changes in chemical bonding. By analyzing the Electron Localization Function (ELF), we can identify regions of highly localized electrons and distinguish between metallic, covalent, and ionic bonds. We compared the ELF distributions around oxygen atoms in the defect-free model and those in the defect-introduced model. Figs. 7a and 7b present the ELF maps before and after the introduction of a 4-coordinated oxygen vacancy, respectively. Prior to defect formation, pronounced regions of strong electron localization are observed between the oxygen atom and its neighboring Al atoms, distributed along the Al–O–Al bond directions. This indicates a high degree of electron localization in these regions, where localized electron pairs are stably formed. After the introduction of the oxygen vacancy, the ELF maps exhibit enhanced local asymmetry, accompanied by a pronounced reduction in the degree of electron localization. This change suggests that the removal of the oxygen atom disrupts the original bonding environment and weakens the localization of electrons in the vicinity of the defect. Figs. 7c and 7d show the ELF around a 3-coordinated oxygen atom before and after vacancy formation, respectively. Upon vacancy formation, the electron localization at the defect site is significantly weakened, and the surrounding regions exhibit pronounced perturbations in the localization pattern. A relatively extended region with low ELF values emerges, indicating a reduction in local electron density and a decrease in electron localization. This behavior suggests that the original Al–O–Al bonding network is disrupted, leading to a redistribution of electronic states without the formation of new strong bonding configurations. Consequently, the electronic states become more delocalized, with a spatially diffuse charge density distribution. Figs. 7e and 7f display the ELF distribution before and after introducing a 2-coordinated V_O . Before defect formation, distinct high-ELF regions (highlighted in red) are observed between the oxygen atom and neighboring Al atoms, reflecting strong electron localization and pronounced Al–O bonding characteristics with a high degree of spatial symmetry. After introducing the V_O , the high-ELF region at the defect site does not exhibit a significant reduction, and a similar strong localized distribution is preserved. This indicates that the electron localization at the vacancy site is not directly destroyed by defect formation. However, substantial changes are

observed in the ELF distribution in the surrounding regions. Some of the originally uniform high-ELF regions are weakened, while several intermediate-ELF regions become asymmetric, reflecting a vacancy-induced non-local reconstruction of the electronic structure. These results suggest that the oxygen vacancy strongly interacts with the surrounding bonding network, driving a rearrangement of the electronic states in its vicinity.

Comparing the total density of states (TDOS) between defect-free and defect-containing models (Fig. 8), we observe that the Fermi level is located near the middle of the band gap in the defect-free model. A finite density of states is present on the valence-band side, whereas the energy range from 0 to approximately +5 eV is nearly devoid of electronic states, with a pronounced increase in the density of states only appearing around +5 eV, close to the conduction band minimum. This behavior is consistent with the intrinsic characteristics of amorphous Al_2O_3 as a wide-bandgap, highly insulating dielectric material. In contrast, upon the introduction of oxygen vacancies, emergent peaks in the electronic density of states are observed in the vicinity of the Fermi level (around 0 eV) for all defective models. This indicates that V_O s introduce new localized electronic states within the pristine band gap, thereby breaking the electronic-state symmetry of the defect-free system. Although the positions and intensities of the defect-related peaks near 0 eV are comparable for the 4- and 3-coordinated V_O models (Figs. 8b and 8c), a more detailed defect-level analysis reveals notable differences. In the 4-coordinated model, the defect states are located closer to the valence band maximum, leading to a higher probability of electron trapping and a reduced ability to release free electrons for conduction. Consequently, the contribution of 4-coordinated V_O s to electrical conductivity enhancement is limited. In contrast, the defect states in the 3-coordinated model lie closer to the Fermi level, while the 2-coordinated model exhibits multiple defect states within the band gap (Fig. 8d). These additional states provide multiple channels for carrier generation and transport, facilitating carrier excitation and enhancing electrical conductivity.

Overall, V_O s introduce new localized states within the band gap of amorphous Al_2O_3 , and the energy distribution and degree of spatial localization of these states are governed by the coordination environment of the vacancy. By modulating carrier generation and localization characteristics, these vacancy-induced states affect the electrical behavior of amorphous Al_2O_3 .

B. Influence of V_O Concentration on Electrical Conductivity

Under irradiation environments, the concentration of V_O defects in amorphous Al_2O_3 increases with increasing irradiation dose, and the defect concentration directly influences the local electronic structure and

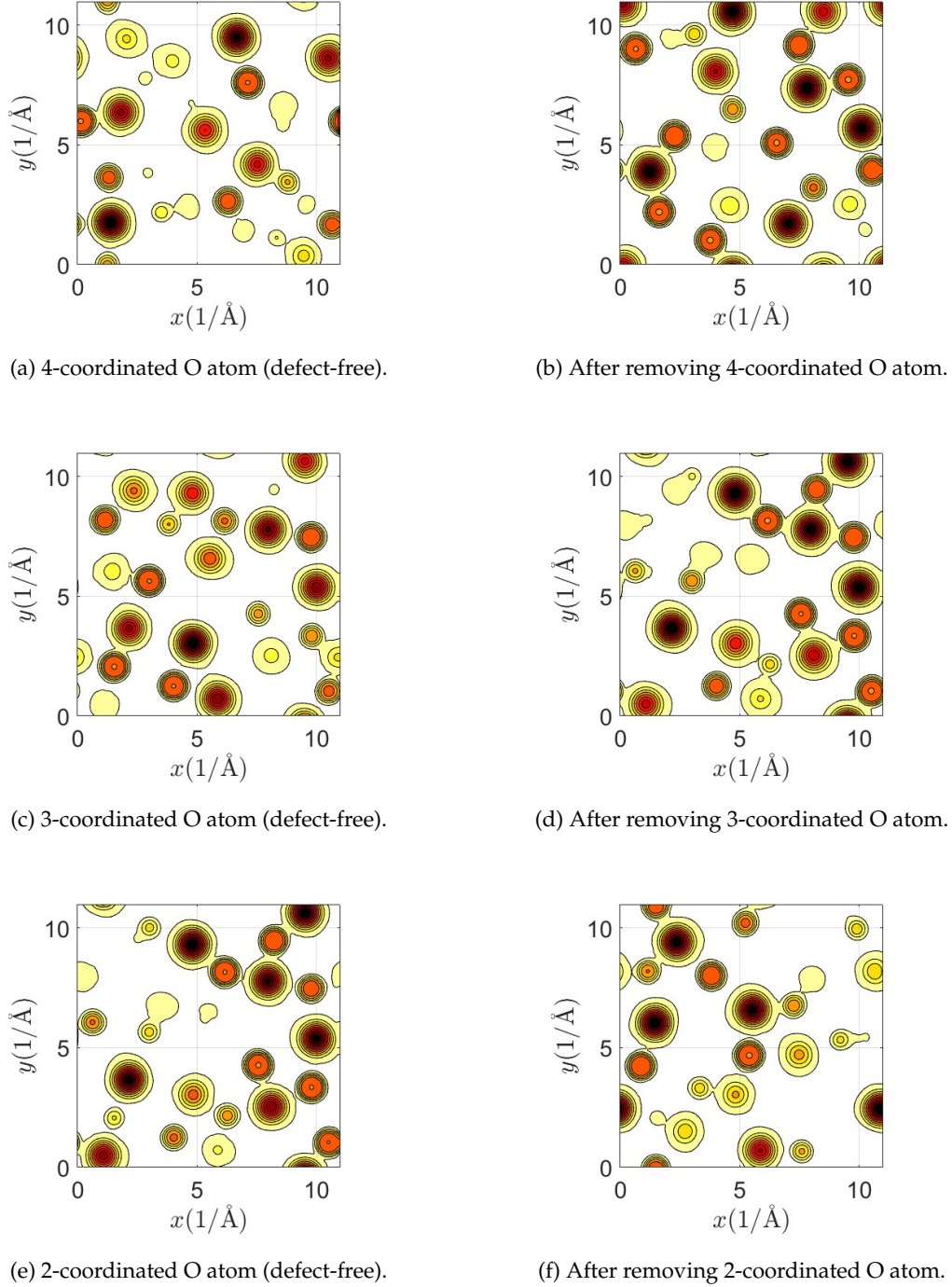


FIG. 6: Electrostatic potential slices for different models ($x = 0$ plane). (a), (c), (e) show electrostatic potential slice centered at the position of the oxygen atom before defect introduction. (b), (d), (f) show electrostatic potential slice near the defect site, centered on the atom nearest to the introduced vacancy.

macroscopic transport properties of the material. To systematically investigate how variations in V_O concentration regulate the electrical conductivity of amorphous Al_2O_3 , we randomly introduced 1, 2, 4, and 9 V_O s into the amorphous Al_2O_3 models to simulate irradiation-

induced defects. The coordination environment of the vacancies was kept fixed to eliminate the influence of coordination-related variations on the transport properties, thereby enabling an isolated assessment of the effect of vacancy concentration.

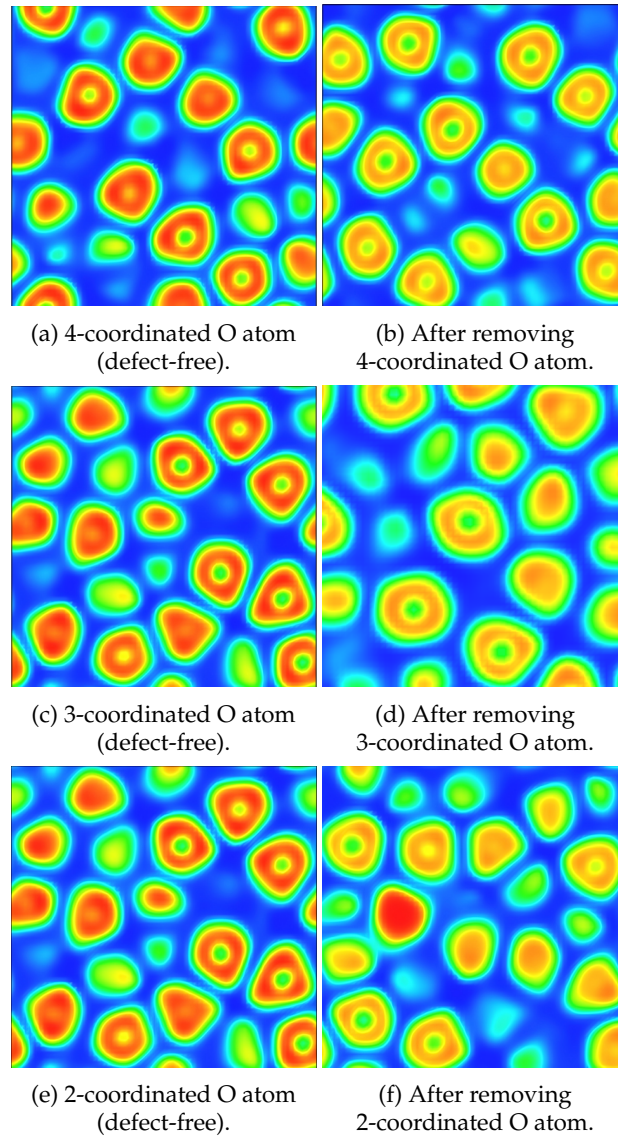


FIG. 7: Electron localization function (ELF) slices for different models. (a), (c), (e) show ELF at the position of the oxygen atom before defect introduction. (b), (d), (f) show ELF near the defect site after vacancy formation.

As shown in Fig. 9, the introduction of a single V_O leads to an enhancement of the electrical conductivity compared with the defect-free model, indicating that an isolated V_O can introduce shallow donor states within the band gap and increase the concentration of free charge carriers. By comparing the conductivity spectra of different models (Fig. 10), we find that the introduction of a single V_O gives rise to a weak peak near the Fermi level (0–1 eV). Consistent with the density-of-states results (Fig. 12), a newly emerged electronic state appears near the Fermi level, in agreement with the defect-level analysis (Fig. 11). This defect state lies close to the conduction band minimum and can be identified as a typical shallow donor level. Such shallow donor states are capable of releasing electrons into the conduction band, thereby increasing the free carrier concentra-

tion and enhancing the probability of electronic transitions. These results indicate that, at low defect concentrations, V_O s primarily act as electron donors, providing additional conductive pathways for the material.

When two V_O s are introduced, the overall conductivity exhibits little change and remains comparable to that of the defect-free model, indicating that the transport properties are only weakly affected. Although a peak near the Fermi level can still be observed in the conductivity spectrum, the presence of two V_O s induces only limited local structural perturbations and does not yet lead to the formation of deep defect levels or vacancy clustering. With further increases in vacancy concentration, the electrical conductivity exhibits a monotonic evolution that is consistent with trends observed in experimental simulations. Upon introducing four

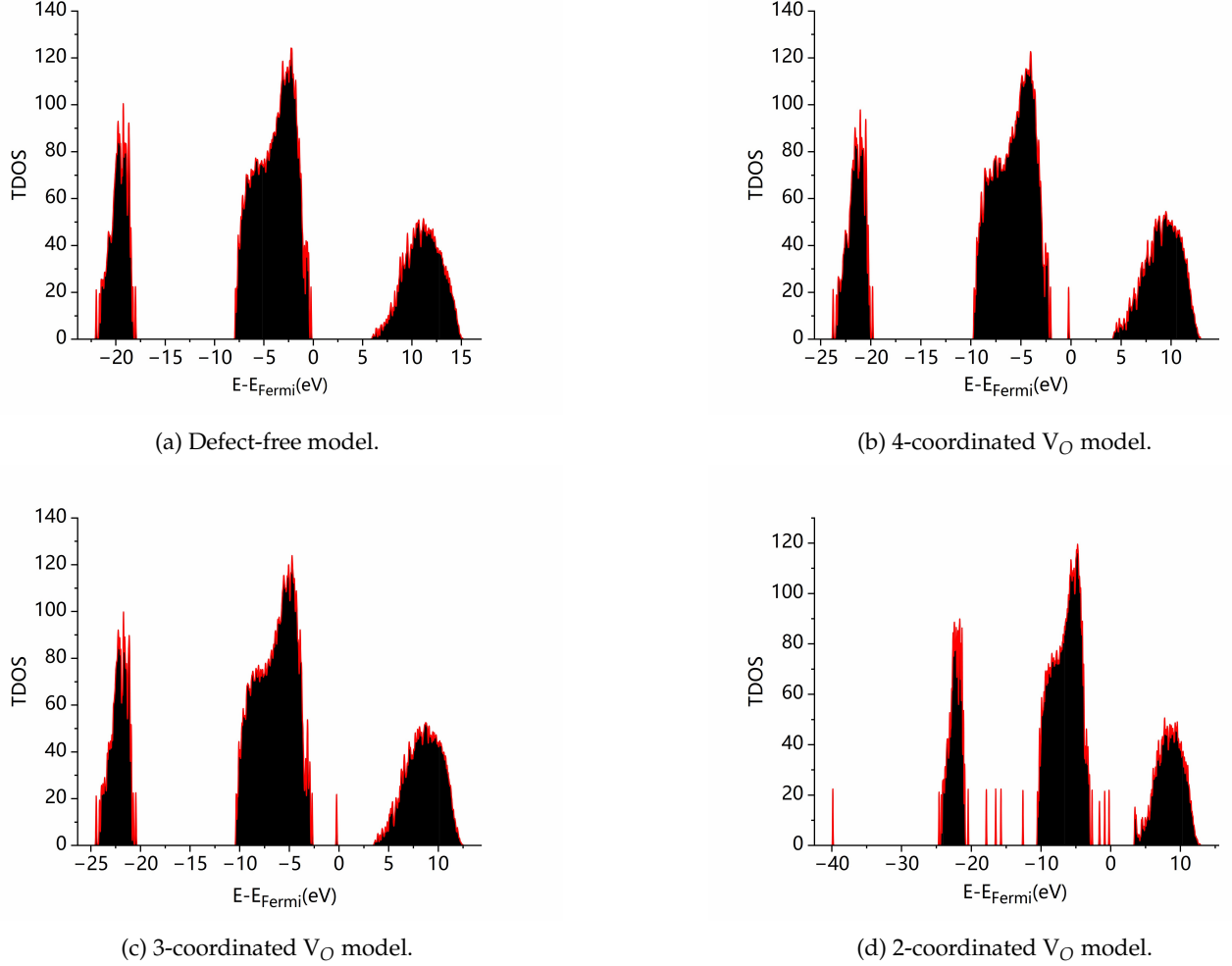


FIG. 8: Total density of states (TDOS) for amorphous Al_2O_3 models with different V_O coordination environments.

V_O s, the conductivity decreases markedly, showing a behavior that is fundamentally different from that observed at low defect concentrations. This suggests that higher concentrations of V_O s tend to introduce deeper donor states, which are less effective at supplying free carriers and may even act as carrier traps, thereby hindering electronic transport. The conductivity spectrum shows a clear overall change, with multiple peaks appearing near the Fermi level and a pronounced reduction in conductivity in the low-energy region. The associated defect levels are predominantly located closer to the valence band (Fig. 11). In addition, interactions between multiple vacancies may lead to defect-defect coupling or the formation of localized vacancy clusters, resulting in repeated carrier scattering within confined regions. Such effects suppress effective conductive channels and impede carrier migration, ultimately leading to degraded transport performance. Therefore, although increasing V_O concentration can introduce more electronic states within the band gap, these states do not necessarily contribute to conduction.

The density-of-states (DOS) results for all models are shown in Fig. 12. With increasing V_O concentration, the number of electronic states within the band gap increases and the effective band gap narrows. In principle, such changes could facilitate electronic excitation and enhance electrical conductivity. However, the calculated conductivity instead decreases, indicating that irradiation-induced high concentrations of V_O s in amorphous Al_2O_3 possess a strong electron-trapping capability. This behavior highlights the distinct influence of high-density V_O s on the band structure and transport properties of amorphous materials.

In amorphous systems, the electrical properties exhibit a nonlinear dependence on V_O concentration. At low defect concentrations, shallow donor states introduced by V_O s enhance electrical conductivity. In contrast, high concentrations of V_O s do not further improve conductivity but instead promote carrier trapping and suppress electron tunneling. As a result, the effective tunneling-blocked junction area increases, leading to a

degradation of the overall transport performance.

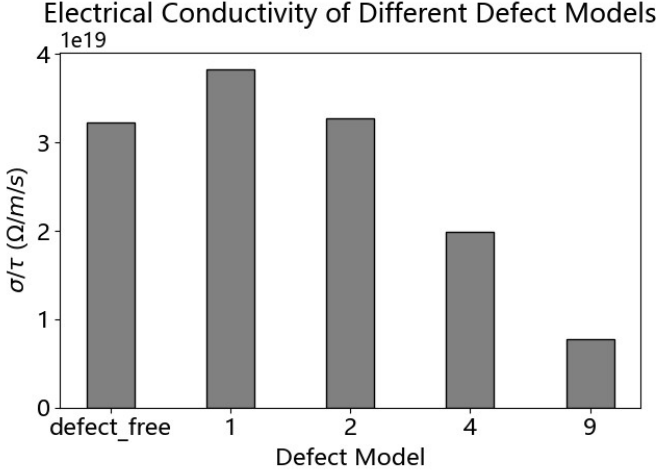


FIG. 9: Electrical conductivity (σ/τ) comparison of amorphous Al_2O_3 models with different numbers of V_{OS} ($N = 0, 1, 2, 4, 9$).

V. IMPACT OF OXYGEN VACANCIES ON JOSEPHSON JUNCTION DECOHERENCE MECHANISMS

A. Decoherence Mechanisms

Since charge transport is intrinsically linked to the critical current of Josephson junctions, conductivity variations induced by V_{OS} can introduce additional low-frequency noise sources. In particular, such defect-induced fluctuations can give rise to critical current noise with a pronounced $1/f$ characteristic near the operating frequencies of superconducting qubits, directly affecting the energy level splitting and phase stability. Therefore, we discuss the mechanisms by which V_{O} defects influence qubit decoherence from both theoretical and numerical perspectives.

According to Van Harlingen et al. [35], the low-frequency $1/f$ noise spectral density of the critical current in Josephson junctions is correlated with the decoherence time of superconducting qubits, as shown in Eq. 1:

$$T_{\phi} \propto \frac{I_0}{\Omega \Lambda \sqrt{S_{I_0}(1 \text{ Hz})}}, \quad (1)$$

where Ω is the tunneling frequency, and $\Omega/2\pi$ is the energy level splitting frequency. For a superconducting qubit, the energy difference between the two quantum states is $\hbar\Omega$.

The parameter Λ represents the relative variation in energy level splitting caused by the relative change of

the critical current,

$$\Lambda = \left| \frac{I_0}{\Omega} \frac{d\Omega}{dI_0} \right|, \quad (2)$$

and indicates the sensitivity of the qubit to fluctuations in critical current. The larger Λ is, the more sensitive the qubit is to critical current fluctuations and the more easily it is affected by decoherence.

The spectral density of critical current noise at 1 Hz can be approximated as

$$S_{I_0}^{1/2}(1 \text{ Hz}) \approx 144 \left(\frac{I_0}{\mu\text{A}} \right) \left(\frac{\mu\text{m}^2}{A} \right)^{1/2} \text{ pA}/\sqrt{\text{Hz}}, \quad (3)$$

where A is the junction area. The decoherence time can be estimated through this spectral density.

The critical current and the junction resistance are linked by the relation

$$I_0 = \frac{\pi\Delta}{2eR_N}, \quad (4)$$

where Δ is the superconducting energy gap, and R_N is the junction resistance.

According to Eq. 4, conductivity fluctuations lead to variations in the junction resistance, thereby influencing the critical current. Such fluctuations induced by V_{OS} can be regarded as the superposition of multiple random telegraph signals [35], forming $1/f$ low-frequency noise that modulates the qubit energy level splitting frequency and consequently reduces the coherence time. Single charge traps generate telegraph noise characterized by two-state lifetimes (occupied/unoccupied), contributing Lorentzian noise peaks with an effective correlation time

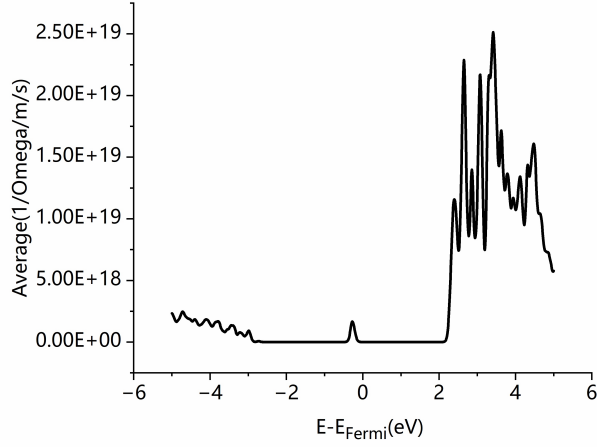
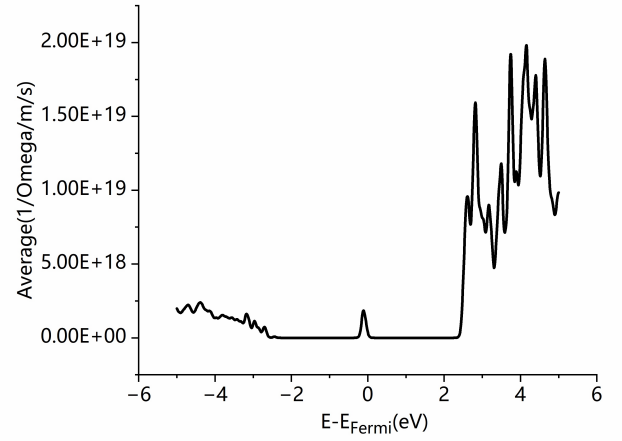
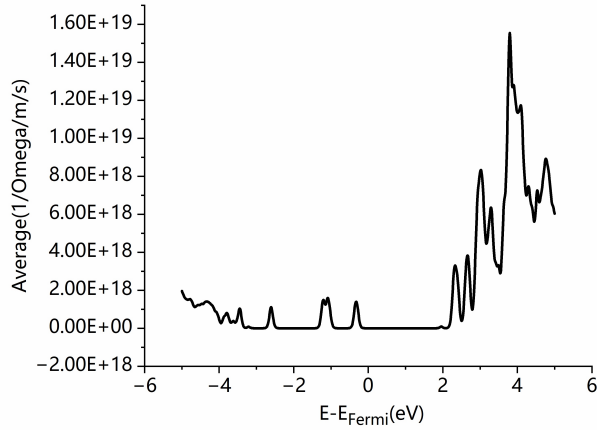
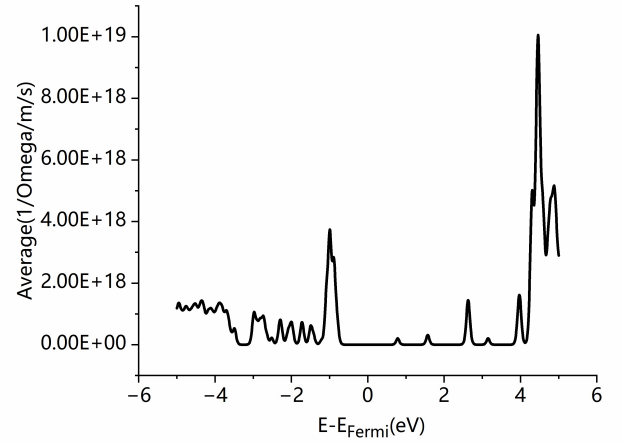
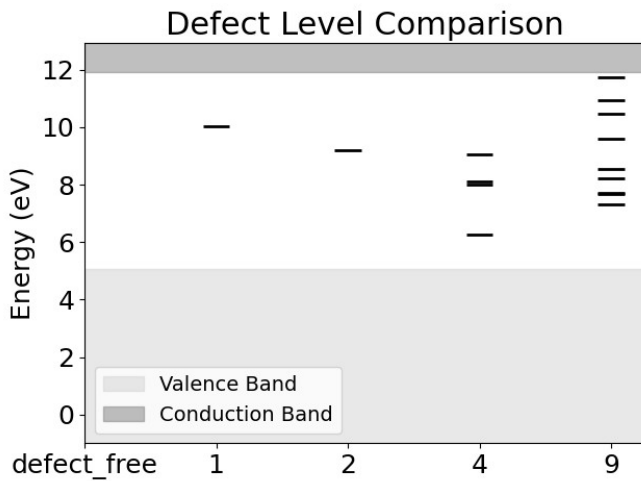
$$\tau_{\text{eff}} = \left(\frac{1}{\tau_t} + \frac{1}{\tau_u} \right)^{-1}. \quad (5)$$

For a junction of area A , the critical current change ΔI_0 is proportional to the effective blocked tunneling area DA by trapped charges,

$$\Delta I_0 = \left(\frac{DA}{A} \right) I_0. \quad (6)$$

If a charge is trapped, the effective junction area blocked for tunneling increases.

The spectral density of the critical current noise induced by a single trap is proportional to $(\Delta I_0)^2$. S_{I_0} is proportional to I_0^2/A . As the irradiation dose increases, multiple V_{O} traps emerge within the oxide barrier, and the superposition of their Lorentzian spectra forms a $1/f$ -like noise spectrum. The spectral density of N iden-

(a) Model with one V_O ($N = 1$).(b) Model with two V_O s ($N = 2$).(c) Model with four V_O s ($N = 4$).(d) Model with nine V_O s ($N = 9$).FIG. 10: Electrical conductivity spectra (σ/τ) for amorphous Al_2O_3 models with different numbers of V_O s.FIG. 11: Defect level distributions for amorphous Al_2O_3 models with different numbers of V_O s.

tical traps is proportional to $N(\Delta I_0)^2$:

$$N(\Delta I_0)^2 = nA \left(\frac{DA}{A} \right)^2 I_0^2, \quad (7)$$

where n denotes the trap density per unit area. Consequently, with increasing irradiation dose, the concentration of V_O defects increases, leading to an enhancement of critical current noise. The enhanced noise spectral density is associated with a shortened decoherence time. The temperature dependence of $1/f$ critical current noise remains inconclusive. Since charge traps predominantly operate via tunneling at low temperatures, the temperature dependence is expected to be weak, and thus the described noise spectral density relation is applicable in our study.

Using the time-domain scan-averaging method and experimental parameters ($I_0 = 1$ mA, $A = 0.01$ mm², $\Lambda = 100$, $\Omega/2\pi = 1$ GHz, $T = 100$ mK), decoherence

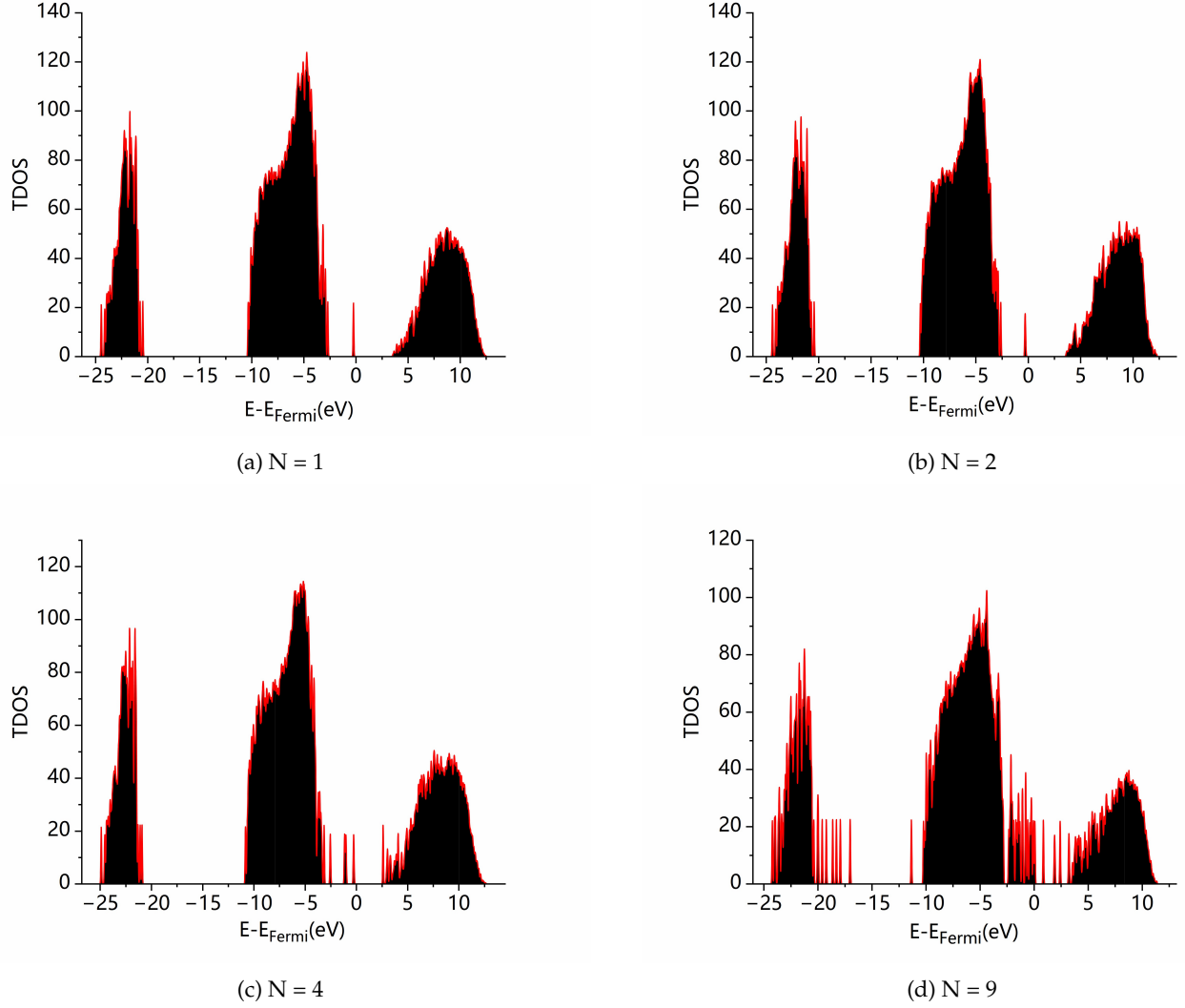


FIG. 12: Total density of states for amorphous Al_2O_3 models with different numbers of V_{O} s.

times are estimated between 0.8 ms and 12 ms (Eq. 8), depending on junction area:

$$t_f^B(\text{ms}) \approx 15 \times A^{1/2}(\mu\text{m}) \times \frac{1}{\Lambda} \times \frac{1}{\Omega(\text{GHz})} \times \frac{T}{4.2\text{K}}. \quad (8)$$

B. Estimation of Decoherence Times for Different Models

To quantitatively evaluate the impact of different types of V_{O} defects on the decoherence performance of superconducting qubits, we estimated the decoherence times for each model based on the critical current noise mechanism proposed by Van Harlingen et al. [35], in conjunction with the conductivity variations obtained in Sec. IV.

Since the exact relaxation time in amorphous Al_2O_3 is difficult to determine, this work focuses on the rela-

tive variation of σ/τ among different vacancy configurations, which reflects the transport changes induced by V_{O} s. As the relaxation time τ is expected to vary weakly among these configurations, it cancels out when considering the relative fluctuations of the critical current; therefore, the decoherence analysis can be performed directly using the calculated σ/τ values.

According to Eq. 4, assuming a fixed superconducting energy gap, the critical current I_0 is proportional to the electrical conductivity:

$$R_N \propto \frac{1}{\sigma}, \quad I_0 \propto \sigma \cdot \Delta. \quad (9)$$

When the conductivity changes, it induces a slight perturbation in the resistance:

$$\frac{\Delta I_0}{I_0} = -\frac{\Delta R_N}{R_N} = \frac{\Delta \sigma}{\sigma}, \quad (10)$$

so that

$$\Delta I_0 \propto \frac{\Delta\sigma}{\sigma}. \quad (11)$$

Therefore, variations in conductivity give rise to corresponding changes in the critical current. As a result, the noise spectral density can be written as

$$S_{I_0}(f) \propto N(\Delta I_0)^2 \propto N\left(\frac{\Delta\sigma}{\sigma}\right)^2, \quad (12)$$

and the decoherence time becomes

$$T_\phi \propto \frac{1}{S_{I_0}(f)} \propto \frac{1}{N(\Delta\sigma/\sigma)^2}. \quad (13)$$

To avoid divergence and to compare relative decoherence times, we employ a phenomenological normalization:

$$T_\phi = \frac{T_{\phi,0}}{1 + N(\Delta\sigma/\sigma_0)^2}, \quad (14)$$

where σ_0 is the conductivity of the defect-free model and $T_{\phi,0}$ is its decoherence time. This expression captures the qualitative trend that larger conductivity fluctuations and higher defect densities reduce coherence.

Based on the derived theoretical framework, the decoherence times of superconducting qubits in the presence of oxygen-vacancy defects can be estimated. Using experimentally relevant parameters and assuming a decoherence time of 1 ms for the defect-free model, the decoherence times for each model are obtained and summarized in Tables II and III. The results are consistent with theoretical expectations and exhibit trends in agreement with experimental observations.

TABLE II: Conductivity σ/τ , relative fluctuation $\Delta\sigma/\sigma_0$, and estimated decoherence time T_ϕ for V_O defect models with different coordination numbers. $\sigma_0 = 3.23 \times 10^{19} \text{ } \Omega^{-1}\text{m}^{-1}\text{s}^{-1}$ is the conductivity of the defect-free model.

Model	$\sigma/\tau (\Omega^{-1}\text{m}^{-1}\text{s}^{-1})$	$\Delta\sigma/\sigma_0$	T_ϕ (ms)
Defect-free	3.23×10^{19}	0	1.000
4-coordinated	2.48×10^{19}	-0.232	0.949
3-coordinated	3.83×10^{19}	+0.186	0.967
2-coordinated	3.51×10^{19}	+0.086	0.993

As can be seen from the data summarized in Tables II and III, both the coordination environment and the concentration of defects have a significant impact on the decoherence time of superconducting qubits. In amorphous Al_2O_3 , the introduction of conventional 4-coordinated V_O s maintains the overall insulating character of the material; however, it leads to the largest con-

TABLE III: Conductivity σ/τ , relative fluctuation $\Delta\sigma/\sigma_0$, and estimated decoherence time T_ϕ for V_O defect models with different numbers of vacancies.

Number of V_O s	$\sigma/\tau (\Omega^{-1}\text{m}^{-1}\text{s}^{-1})$	$\Delta\sigma/\sigma_0$	T_ϕ (ms)
0	3.23×10^{19}	0	1.000
1	3.83×10^{19}	+0.186	0.967
2	3.27×10^{19}	+0.012	0.999
4	1.99×10^{19}	-0.380	0.634
9	7.78×10^{18}	-1.400	0.053

ductivity fluctuations, resulting in the shortest decoherence time. In contrast, 3- and 2-coordinated V_O s increase the conductivity while inducing relatively smaller conductivity fluctuations, and consequently cause a less pronounced reduction in the decoherence time compared with the 4-coordinated case. As the number of V_O s increases, except for anomalous behavior observed at low defect concentrations, the conductivity exhibits a decreasing trend, while the amplitude of conductivity fluctuations increases with defect concentration. Correspondingly, the decoherence time decreases rapidly as the vacancy concentration increases. These results indicate that, under irradiation conditions, a higher density of oxygen-vacancy defects in superconducting qubits leads to shorter decoherence times and more severe degradation of device performance. This trend is consistent with experimental observations.

C. Impact on Rabi Oscillations

To illustrate how the estimated decoherence times affect the coherent dynamics of a superconducting qubit, we simulate Rabi oscillations—the coherent oscillations of the qubit state under resonant microwave driving. The excited-state probability of a qubit undergoing Rabi oscillations with decoherence time T_2 is given by

$$P_{\text{ex}}(t) = \frac{1}{2} \left[1 - e^{-t/T_2} \cos(\Omega_R t) \right], \quad (15)$$

where Ω_R is the Rabi frequency. For a typical Rabi frequency $\Omega_R/2\pi = 2$ MHz, we plot the envelope of $P_{\text{ex}}(t)$ (i.e., the curves $\frac{1}{2}[1 \pm e^{-t/T_2}]$) for the decoherence times obtained from our models (Tables II and III). The time window extends to 200 μs , corresponding to roughly $4T_2$ for the shortest coherence time ($T_2 = 0.053$ ms) and $0.2T_2$ for the longest ($T_2 = 1.000$ ms).

Figure 13 clearly demonstrates that even modest reductions in T_2 (e.g., 0.949 ms for a 4-coordinated vacancy) cause noticeable narrowing of the envelope, corresponding to faster decay of the oscillation amplitude. When the vacancy concentration increases (e.g., nine

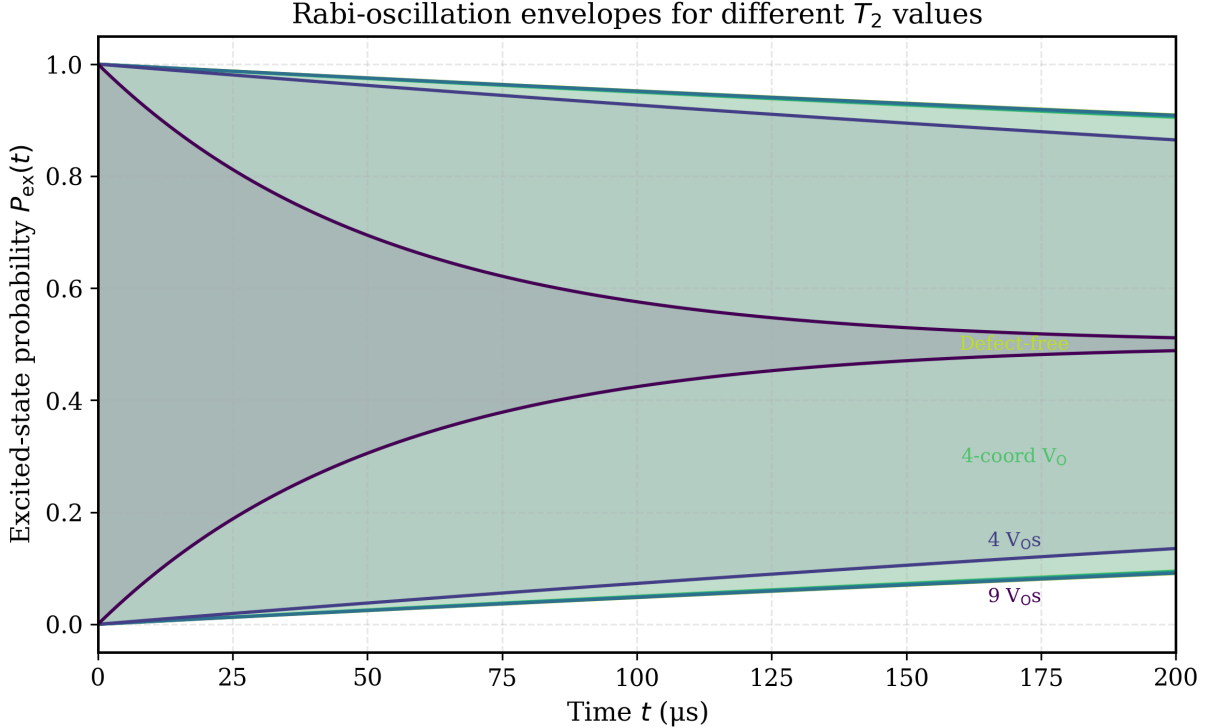


FIG. 13: Envelope of Rabi oscillations for different decoherence times T_2 estimated from the V_O defect models. The shaded region between the upper and lower envelopes ($\frac{1}{2}[1 \pm e^{-t/T_2}]$) indicates the range of the oscillating probability $P_{\text{ex}}(t)$. The defect-free case ($T_2 = 1.000$ ms) shows almost no damping over the simulated $200 \mu\text{s}$ window, while the model with nine V_{OS} ($T_2 = 0.053$ ms) exhibits nearly complete damping within $\sim 50 \mu\text{s}$. Intermediate vacancy configurations (4-coordinated V_O , $T_2 = 0.949$ ms; 4 V_{OS} , $T_2 = 0.634$ ms) display progressively stronger damping. The plot directly visualizes how oxygen-vacancy-induced conductivity fluctuations degrade qubit coherence and limit the number of coherent gate operations that can be performed.

V_{OS} , $T_2 = 0.053$ ms), the envelope collapses within $\sim 50 \mu\text{s}$, meaning the Rabi oscillations are almost completely suppressed after a few tens of microseconds. This illustrates that the conductivity fluctuations induced by oxygen vacancies not only shorten the decoherence time but also directly degrade the qubit's ability to sustain coherent gate operations. Therefore, controlling V_O formation—both coordination environment and concentration—is critical for maintaining high-fidelity quantum gates in superconducting quantum processors, especially in radiation-prone environments.

VI. CONCLUSION

In summary, by constructing amorphous Al_2O_3 models containing oxygen-vacancy defects with different coordination environments and concentrations, this work employs DFT calculations to systematically investigate the influence of V_{OS} on the electrical properties of the material. The results show that both the coordination environment and the concentration of V_{OS} play a key role in determining the electrical behavior of amorphous

Al_2O_3 .

Compared with the defect-free model, the 4-coordinated V_O induces pronounced conductivity fluctuations, leading to a substantial reduction in the coherence time of the qubit. In contrast, 2- and 3-coordinated V_{OS} tend to introduce shallow donor states, which enhance the electrical conductivity while causing relatively smaller conductivity fluctuations. Moreover, the concentration of V_{OS} exhibits a nonlinear modulation effect on the electrical properties, and as the defect density increases, the amplitude of conductivity fluctuations grows, resulting in progressively shorter coherence times of the qubit.

Overall, this work provides a comprehensive analysis of the effects of irradiation-induced V_{OS} in the amorphous Al_2O_3 tunnel barrier of Josephson junctions on both the electrical properties of the material and the coherence of the qubit. Our findings emphasize the importance of controlling V_O formation—both in terms of coordination environment and concentration—for improving the radiation tolerance and coherence performance of superconducting quantum devices. Future work could involve experimental validation of

these predictions through controlled irradiation experiments and noise measurements. Additionally, multi-scale modeling that connects atomistic defect structures to device-level noise characteristics, as well as explor-

ing alternative barrier materials or defect-engineering strategies (such as doping or passivation), may offer pathways to further enhance qubit coherence under irradiation environments.

-
- [1] M. A. Nielsen and I. L. Chuang, *Quantum computation and quantum information* (Cambridge university press, 2010).
- [2] B. C. Sanders, Superconducting quantum computing beyond 100 qubits, *Physics* **18**, 45 (2025).
- [3] J. Koch, T. M. Yu, J. Gambetta, A. A. Houck, D. I. Schuster, J. Majer, A. Blais, M. H. Devoret, S. M. Girvin, and R. J. Schoelkopf, Charge-insensitive qubit design derived from the cooper pair box, *Physical Review A—Atomic, Molecular, and Optical Physics* **76**, 042319 (2007).
- [4] D. A. Bennett, L. Longobardi, V. Patel, W. Chen, D. V. Averin, and J. E. Lukens, Decoherence in rf squid qubits, *Quantum Information Processing* **8**, 217 (2009).
- [5] G. Catelani, S. E. Nigg, S. M. Girvin, R. J. Schoelkopf, and L. I. Glazman, Decoherence of superconducting qubits caused by quasiparticle tunneling, *Physical Review B—Condensed Matter and Materials Physics* **86**, 184514 (2012).
- [6] X. Pan, Y. Zhou, H. Yuan, L. Nie, W. Wei, L. Zhang, J. Li, S. Liu, Z. H. Jiang, G. Catelani, *et al.*, Engineering superconducting qubits to reduce quasiparticles and charge noise, *Nature Communications* **13**, 7196 (2022).
- [7] Y. Shalibo, Y. Rofe, D. Shwa, F. Zeides, M. Neeley, J. M. Martinis, and N. Katz, Lifetime and coherence of two-level defects in a josephson junction, *Physical review letters* **105**, 177001 (2010).
- [8] S. Choi, Localization of metal-induced gap states at the metal-insulator interface: Origin of flux noise, (2010).
- [9] C. Müller, A. Shnirman, and Y. Makhlin, Relaxation of josephson qubits due to strong coupling to two-level systems, *Physical Review B—Condensed Matter and Materials Physics* **80**, 134517 (2009).
- [10] A. M. Holder, K. D. Osborn, C. Lobb, and C. B. Musgrave, Bulk and surface tunneling hydrogen defects in alumina, *Physical review letters* **111**, 065901 (2013).
- [11] L. Gordon, H. Abu-Farsakh, A. Janotti, and C. G. Van de Walle, Hydrogen bonds in al₂o₃ as dissipative two-level systems in superconducting qubits, *Scientific reports* **4**, 7590 (2014).
- [12] D. Bafia, A. Murthy, A. Grassellino, and A. Romanenko, Oxygen vacancies in niobium pentoxide as a source of two-level system losses in superconducting niobium, *Physical Review Applied* **22**, 024035 (2024).
- [13] Z. Guo, F. Ambrosio, and A. Pasquarello, Oxygen defects in amorphous al₂o₃: A hybrid functional study, *Applied physics letters* **109** (2016).
- [14] J. Qiu, S. Wang, H. Sun, C. Han, and Z. Shan, Manipulation of electrical performance in al-based josephson junctions via oxygen vacancies in barrier, *Journal of Materials Chemistry C* **12**, 19063 (2024).
- [15] Y.-H. Ji, Investigation of decoherence of superconducting charge qubit entangled with the environment, *International Journal of Theoretical Physics* **47**, 2363 (2008).
- [16] P. Koppinen, L. Väistö, and I. Maasilta, Complete stabilization and improvement of the characteristics of tunnel junctions by thermal annealing, *Applied physics letters* **90** (2007).
- [17] N. D. Korshakov, D. O. Moskalev, A. A. Soloveva, D. A. Moskaleva, E. S. Lotkov, A. R. Ibragimov, M. V. Androschuk, I. A. Ryzhikov, Y. V. Panfilov, and I. A. Rodionov, Aluminum josephson junction microstructure and electrical properties modified by thermal annealing, *Scientific Reports* **14**, 26066 (2024).
- [18] C. Müller, J. H. Cole, and J. Lisenfeld, Towards understanding two-level-systems in amorphous solids: insights from quantum circuits, *Reports on Progress in Physics* **82**, 124501 (2019).
- [19] M. Ding, Damage effect of al₂o₃ based metal-oxide-semiconductor structures under gamma-ray irradiation, *Micromachines* **12**, 661 (2021).
- [20] M. Ding, Y. Cheng, X. Liu, and X. Li, Total dose response of hafnium oxide based metal-oxide-semiconductor structure under gamma-ray irradiation, *IEEE Transactions on Dielectrics and Electrical Insulation* **21**, 1792 (2014).
- [21] H. Zhu, Z. Zheng, B. Li, B. Li, G. Zhang, D. Li, J. Gao, L. Yang, Y. Cui, C. Liang, *et al.*, Total dose effect of al₂o₃-based metal-oxide-semiconductor structures and its mechanism under gamma-ray irradiation, *Semiconductor Science and Technology* **33**, 115010 (2018).
- [22] G. Kresse and J. Hafner, Ab initio molecular dynamics for liquid metals, *Physical review B* **47**, 558 (1993).
- [23] G. Kresse and J. Furthmüller, Efficient iterative schemes for ab initio total-energy calculations using a plane-wave basis set, *Physical review B* **54**, 11169 (1996).
- [24] P. E. Blöchl, Projector augmented-wave method, *Physical review B* **50**, 17953 (1994).
- [25] G. Kresse and D. Joubert, From ultrasoft pseudopotentials to the projector augmented-wave method, *Physical review b* **59**, 1758 (1999).
- [26] J. Sun, A. Ruzsinszky, and J. P. Perdew, Strongly constrained and appropriately normed semilocal density functional, *Physical review letters* **115**, 036402 (2015).
- [27] J. Heyd, G. E. Scuseria, and M. Ernzerhof, Hybrid functionals based on a screened coulomb potential, *The Journal of chemical physics* **118**, 8207 (2003).
- [28] H. J. S. Ge and M. Ernzerhof, Erratum: “hybrid functionals based on a screened coulomb potential” [j. chem. phys. **118**, 8207 (2003)], *J. Chem. Phys* **124**, 219906 (2006).
- [29] E. O. Filatova and A. S. Konashuk, Interpretation of the changing the band gap of al₂o₃ depending on its crystalline form: connection with different local symmetries, *The Journal of Physical Chemistry C* **119**, 20755 (2015).
- [30] A. Pugliese, B. Shyam, G. M. Repa, A. H. Nguyen, A. Mehta, E. B. Webb III, L. A. Fredin, and N. C. Strandwitz, Atomic-layer-deposited aluminum oxide thin films probed with x-ray scattering and compared to molecular dynamics and density functional theory models, *ACS omega* **7**, 41033 (2022).
- [31] G. Gutierrez and B. Johansson, Molecular dynamics study of structural properties of amorphous al₂o₃, *Physical*

- review B **65**, 104202 (2002).
- [32] V. Van Hoang and S. K. Oh, Simulation of structural properties and structural transformation of amorphous Al_2O_3 , *Physica B: Condensed Matter* **352**, 73 (2004).
- [33] P. Lamparter and R. Kniep, Structure of amorphous Al_2O_3 , *Physica B: Condensed Matter* **234**, 405 (1997).
- [34] Y. Oka, T. Takahashi, K. Okada, and S.-i. Iwai, Structural analysis of anodic alumina films, *Journal of Non-Crystalline Solids* **30**, 349 (1979).
- [35] D. Van Harlingen, T. Robertson, B. Plourde, P. Reichardt, T. Crane, and J. Clarke, Decoherence in Josephson-junction qubits due to critical-current fluctuations, *Physical Review B—Condensed Matter and Materials Physics* **70**, 064517 (2004).